Effect of shape on inertial particle dynamics in a channel flow

D.O. Njobuenwu and M. Fairweather

Institute of Particle Science and Engineering, School of Process, Environmental and Materials Engineering, University of Leeds, Leeds LS2 9JT, UK

Phone: +441133432351

Email: d.o.njobuenwu@leeds.ac.uk

Abstract

Particle dynamics in a channel flow are investigated using large eddy simulation and a Lagrangian particle tracking technique. Following validation of single-phase flow predictions against DNS results, fluid velocities are subsequently used to study the behaviour of particles of differing shape assuming one-way coupling between the fluid and the particles. The influence of shape- and orientation-dependent drag and lift forces on both the translational and rotational motion of the particles is accounted for to ensure accurate representation of the flow dynamics of non-spherical particles. The size of the particles studied was obtained based on an equivalent-volume sphere, and differing shapes were modelled using super-quadratic ellipsoid forms by varying their aspect ratio, with their orientation predicted using the incidence angle between the particle relative velocity and the particle principal axis. Results are presented for spherical, needle- and platelet-like particles at a number of different boundary layer locations along the wall-normal direction within the channel. The time evolution and probability density function of selected particle translational and rotational properties show a clear distinction between the behaviour of the various particles types, and indicate the significance of particle shape when modelling many practically relevant flows.

Keywords: Large eddy simulation, particle, shape, orientation, quaternion

1 Introduction

Particle-laden turbulent flows occur in numerous industrial, environmental and biomedical applications and processes, with most of the particles of practical interest being non-spherical and of various aspect ratios. Although a considerable number of papers have appeared on the motion of particles in channel flow, the focus has in general been on the forces acting on spherical particles and the exchange of momentum between the particles and the carrier fluid. For the dynamics of non-spherical particles, the most common assumption is to use volume equivalent diameters and shape factors to modify the drag coefficient of a sphere, neglecting the associated rotational motion and the torques inherent in the motion of non-spherical particles. This approach is common in commercial computation fluid dynamic codes. This over-simplifies the problem, however, and is not able to accurately predict the motion of large non-spherical particles and their interaction with the carrier flow [1]. Greater success has been achieved [1, 2] when the complete behaviour of non-spherical particles in turbulent flow is accounted for, with this requiring that (i) the lift and drag forces as a function of particle size, shape and orientation, (ii) the rotational motion caused by different torque terms and (iii) particle preferential orientation all be addressed.

Numerical studies on the dynamics of non-spherical particles are rather scarce. Yin et al. [1, 2] considered shape factor- and orientation-dependent drag and lift forces, and particle rotation, in modelling biomass as cylindrical particles in the design of wall-fired burners using co-firing of biomass. The authors implemented a modified Ganser [3] drag coefficient, where the particle size was quantified using the equivalent volume diameter, the particle shape characterized using the particle sphericity, and the aspect ratio, and the orientation dependence accounted for by using the projected area. The profile lift coefficient considered was proportional to the drag and the dependence on the orientation was given by the so-called 'cross-flow principle' [4]. Yin et al. [2] validated their model by comparing its predictions with data from experimental studies of the motion of a cylindrical PVC particle in initially stagnant water, in which the undisturbed water became non-uniform under the effect of the settling of a large PVC particle. The authors [2] reported excellent agreement with data, while Yin et al. [1] found that the cylindrical particle trajectories differ significantly from those of perfect spheres of the same equivalent diameter.

Zastawny et al. [5] investigated the effect of the shape of spheroidal particles with aspect ratios of 1.25, 2.5 and 5.0. The authors derived correlations of drag, lift and torque coefficients based on the models applied in [1, 2], and direct numerical simulations. They reported that for a flow with a shear Reynolds number of 300, the drag coefficient of a prolate spheriod with an aspect ratio of 1.25 increases by up to 20% (depending on the orientation to the flow) compared to the drag coefficient of a sphere. For a prolate spheroid with an aspect ratio of 2.5, the authors reported that the drag coefficient could decrease by up to 37%, and increase by up to 75%, depending on the orientation of the flow. Zastawny et al.'s [5] application of DNS for non-spherical particles further validated the models and algorithms used in [1, 2], demonstrating that such models can be applied to both cylindrical and ellipsoidal particles.

Marchioli et al. [6] analysed the dynamics of fibres dispersed in a low Reynolds number channel flow. Prolate ellipsoidal particles with varying aspect ratio E (a measure of their elongation) and Stokes number (a measure of their inertia) were used to simulate the deposition of rigid elongated fibres. The authors observed that quantitative properties of the fibres' motion differed significantly when compared with those of spheres with equal Stokes number.

Tian et al. [7] studied the transport and deposition of ellipsoidal fibres with different sizes and aspect ratios in a circular pipe flow in the laminar flow regime. The authors also studied the effectiveness of using available equivalent sphere formulations for characterizing the motion of ellipsoidal fibre particles in the laminar flow. These formulations were all based on the concept that the average mobility of the fibre can be expressed in terms of the mobility of its three principal directions. The frequently used equivalent spheres examined in [7] were the equivalent volume diameter sphere, the equivalent Stokes sphere and the equivalent aerodynamic sphere. The authors reported good agreement between their model predictions of fibre deposition in these flows and experimental measurements, as well as with available empirical correlations. Both the particle aspect ratio and the equivalent sphere formulation were found to have a significant influence on the fibres' motion and deposition.

In summary, Yin et al. [1, 2] focused on cylindrical particles in a stagnant flow field, while Marchioli et al. [6] and Tian et al. [7] considered prolate spheroids in low Reynolds number flow, based on the approach of Zhang et al. [8]. Additionally, Zastawny et al. [5] also considered a range of prolate spheroids. To the authors' knowledge, there are no works on particles with a wide range of aspect ratios involving oblate, spherical and prolate spheres in moderate or high Reynolds number flows.

In this work, therefore, both the translational and rotational motions of oblate and prolate spheres are used to study non-spherical particle behaviour in a turbulent channel flow. This involves solution for both the linear and angular momentum of the particles using shape- and orientation-dependent drag and lift coefficients. The predictive approach developed is of particular relevance to nuclear reactor applications where, for example, corrosion products from boiling water reactor components can be transported into the reactor core by the cooling water, where they can deposit on the outside of fuel pins to form CRUD (an acronym for Chalk River unidentified deposit or corrosion residual unidentified deposit). Due to its low thermal conductivity, once deposited CRUD can additionally interfere with cooling water circulation, and hence be responsible for local temperature increases that can further accelerate CRUD formation rates, leading to localised corrosion-induced failures. Also, if these radioactive deposits break loose and circulate through the plant, they can ultimately result in safety hazards for plant workers. Individual CRUD particles are small, from 0.1-2.0 μm, but these generally agglomerate into larger inertial particles with a wide range of sizes and morphologies, varying from needle-like, through near-spherical to platelets or flakes [9].

These particles are modelled in the present work as non-spherical particles using super-quadratic ellipsoid forms [10], parameterised by a, b, c and $E=c/a$; respectively representing the aspect ratios in the x, y and z directions in the

canonical frame of the particle, an index, and the aspect ratio defined as the ratio of the parallel and normal particle diameters [11]. Three special cases of super-ellipsoids are considered: a sphere, and oblate and prolate spheroids, as illustrated in Table 1, with the latter representing platelet (disk) and rod-like (needle) particles, respectively [11].

Table 1: Particle shapes used in the simulations based on super-quadratic forms.

$$\left(\frac{x}{a}\right)^2 + \left(\frac{y}{b}\right)^2 + \left(\frac{z}{c}\right)^2 = 1$$

Sphere	Oblate	Prolate
$a = b = c;\ \ E = 1$	$a = b > c;\ \ E < 1$	$a = b < c;\ \ E > 1$

2 Equations of Motion

2.1 Large eddy simulation

The continuity and Navier-Stokes conservation equations for mass and momentum are decomposed into resolved (large-scale) and unresolved (sub-grid scale) fields using a top-hat filter as this fits naturally into the finite-volume formulation used for solution. The filtered forms of these equations for the resolved scales are given by:

$$\frac{\partial \overline{u}_j}{\partial x_j} = 0 \, , \tag{1}$$

$$\frac{\partial \overline{u}_i}{\partial t} + \overline{u}_j \frac{\partial \overline{u}_i}{\partial x_j} = -\frac{1}{\rho}\frac{\partial \overline{p}}{\partial x_i} - \frac{\partial}{\partial x_j}\left(\overline{\sigma}_{ij} + \tau_{ij}\right), \tag{2}$$

where $\overline{\sigma}_{ij} = -2\nu \overline{s}_{ij}$ and $\tau_{ij} = \overline{u_i u_j} - \overline{u}_i \overline{u}_j$ represent the kinematic viscous stress and sub-grid scale (SGS) stress tensors, respectively. The unknown sub-grid scale stress term required to close these equations was modelled using a dynamic approach [12] which represents the SGS stress as the product of a SGS viscosity and the resolved part of the strain tensor, and is based on the possibility of allowing different values of the Smagorinsky constant at different filter levels. Test-filtering was performed in all space directions, with no averaging of the computed model parameter field.

2.2 Kinematics

A schematic diagram of an ellipsoidal particle and the corresponding frames of reference are shown in Fig. 1 (left), where $\mathbf{x} = [x, y, z]$ are the inertial co-ordinates, $\mathbf{x}' = [x', y', z']$ is the particle co-ordinate system with its origin at the

4

particle centroid and its axis being the principal axis, and $\mathbf{x}'' = [x'', y'', z'']$ is the co-moving co-ordinate system with its origin coinciding with the particle centroid, and its axes being parallel to the inertial frame of reference. The transformation between the co-moving frame and the particle co-ordinates is expressed as $\mathbf{x}' = \mathbf{A} \cdot \mathbf{x}''$ [13]. The transformation matrix $\mathbf{A} = [a_{ij}]$ can be expressed in terms of either Euler angles or quaternions [13]. The Euler angles represent the direction cosines of the particle axes in the inertial frame, as shown in Fig. 1 (left).

Previous investigations, e.g. [8], have shown that the use of Euler angles is very inefficient because of the singularity problem that occurs whenever the azimuthal angle of the particle is 0 or π. The use of the four Euler quaternions overcomes this problem, with the particle rotational dynamics determined in terms of the Euler quaternions $\mathbf{q} = (q_1, q_2, q_3, q_0)$, provided the quaternions satisfy the equality $q_1^2 + q_2^2 + q_3^2 + q_0^2 = 1$. The orientational matrix $\mathbf{A} = A(\mathbf{q})$ in terms of the quaternion $\mathbf{q}$ is given by:

$$\mathbf{A} = A(\mathbf{q}) = \begin{bmatrix} 1 - 2(q_2^2 + q_3^2) & 2(q_1 q_2 + q_3 q_0) & 2(q_1 q_3 - q_2 q_0) \\ 2(q_2 q_1 - q_3 q_0) & 1 - 2(q_3^2 + q_1^2) & 2(q_2 q_3 + q_1 q_0) \\ 2(q_3 q_1 + q_2 q_0) & 2(q_3 q_2 - q_1 q_0) & 1 - 2(q_1^2 + q_2^2) \end{bmatrix} \tag{3}$$

where the individual quaternions are obtained from the Euler angles as:

$$q_1 = \cos \frac{\phi - \psi}{2} \sin \frac{\theta}{2}, \qquad q_2 = \sin \frac{\phi - \psi}{2} \sin \frac{\theta}{2}$$

$$q_3 = \sin \frac{\phi + \psi}{2} \cos \frac{\theta}{2}, \qquad q_0 = \cos \frac{\phi + \psi}{2} \cos \frac{\theta}{2} \tag{4}$$
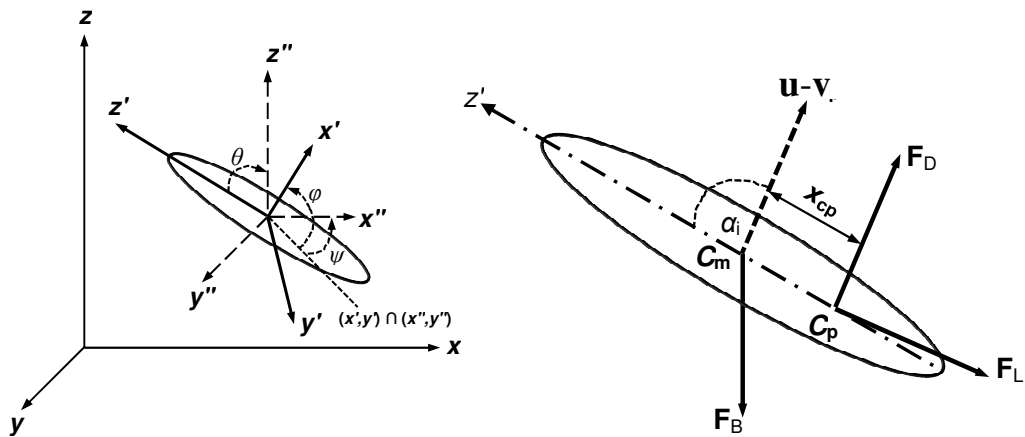

Figure 1: Schematic of co-ordinate system and orientational angles of particle with respect to particle major axis z' (left), and distance between centres of pressure (C_p) and of mass (C_m) of particle, x_{cp}, and incidence angle between (u-v) and particle major axis z', α_i (right).

2.3 Translational and rotational dynamics

A force **F** applied on a particle away from its centroid simultaneously changes two properties of the particle: the linear motion of the centroid and the angular motion around the centroid. The former is governed by the Newtonian equation:

$$\frac{d\mathbf{x}_p}{dt} = \mathbf{v} \tag{5}$$

$$m_p \frac{d\mathbf{v}}{dt} = \mathbf{F}_D + \mathbf{F}_L \tag{6}$$

where $\mathbf{x}_p = [x_p, y_p, z_p]$ and $\mathbf{v} = [v_x, v_y, v_z]$ represent the particle position and velocity vector, respectively, m_p is the mass of the particle, $\mathbf{F}_D$ and $\mathbf{F}_L$ represent the drag and profile lift forces acting on the particle, and t is time. The effect of gravity was not of interest, hence it was neglected. The aim was therefore to minimise the number of degrees of freedom by keeping the simulation setting as simple as possible, and to allow particle interaction with the flow structures alone to influence the particle motion (as employed by a number of authors, e.g. [6]). The drag and profile lift forces resulting from particle orientation are given, according to [2], as:

$$\mathbf{F}_D = \tfrac{1}{2} \rho_f A_D C_D \,|\,\mathbf{u} - \mathbf{v}\,|\,(\mathbf{u} - \mathbf{v}) \tag{7}$$

$$\mathbf{F}_L = \tfrac{1}{2} \rho_f A_L C_L \frac{\mathbf{z}'.(\mathbf{u} - \mathbf{v})}{|\,\mathbf{u} - \mathbf{v}\,|} \big[\mathbf{z}' \times (\mathbf{u} - \mathbf{v})\big] \times (\mathbf{u} - \mathbf{v}) \tag{8}$$

where $\mathbf{u} = (u_x, u_y, u_z)$ is the fluid velocity vector at the particle centroid, z' is the direction of the particle major axis in the inertial frame, and A_D and A_L are the particle areas normal to the direction of the drag and lift forces, respectively. The effective areas A_D and A_L can be expressed as a function of the particle incidence angle, α_i, between the particle slip velocity, (**u**-**v**), and the particle principal axis, z', see Fig. 1 (right), as [2]:

$$A_D = \pi a^2 \left[\cos^2 \alpha_i + \left(\frac{4c}{a\pi}\right)^2 \sin^2 \alpha_i \right]^{\frac{1}{2}} \tag{9}$$

$$A_L = \pi a^2 \left[\sin^2 \alpha_i + \left(\frac{4c}{a\pi}\right)^2 \cos^2 \alpha_i \right]^{\frac{1}{2}} \tag{10}$$

The drag coefficient C_D has been measured for a wide range of particle shapes, but is not commonly available in terms of a functional relationship with the Reynolds number, and the orientation and geometric parameters of the particle for which it ideally should be. One way to deal with this problem is by using the sphericity factor, S, and the volume equivalent diameter, d_{Veq}, as geometric parameters and introducing orientation dependency in drag correlations using the effective area normal to the direction of the drag force. Chhabra et al. [14] compared five of the most promising drag coefficient correlations with data, considering 1900

6

experimental data covering a wide range of particle shapes and hydrodynamic conditions. Based on the overall mean and maximum percentage errors, these authors recommended that the drag expression proposed by Ganser [3] is the most appropriate method for determining C_D, with this expression having an overall error, against those data, of only 16%. The Ganser [3] drag coefficient expression is therefore used for C_D in Eq. (7), as given by:

$$\frac{C_D}{K_2} = \frac{24}{Re_p K_1 K_2}\left[1 + 0.118\left(Re_p K_1 K_2\right)^{0.6567}\right] + \frac{0.4305}{1 + 3305/(Re_p K_1 K_2)} \quad (11)$$

$$K_1 = \left[\frac{d_n}{3d_{Veq}} + \frac{2}{3S^{\frac{1}{2}}}\right]^{-1}, \qquad K_2 = 10^{1.8148(-\log S)^{0.5743}} \quad (12)$$

where $Re_p = |\mathbf{u} - \mathbf{v}|\, d_{Veq}/\nu$, and K_1 and K_2 are coefficients that model the particle shape for spherical particles, or the particle sphericity and orientation for non-spherical particles. $d_n = (4A_D/\pi)^{0.5}$ is the equal-projected area circle diameter. The particle orientation is accounted for in the drag force in Eq. (7) by A_D, the particle projected area normal to the direction of the drag, and by the drag coefficient C_D. The projected area on which the drag is based, given in Eq. (9), is expressed as a functional relationship of the incidence angle α_i and the particle's dimensions a, c. Using an analogy from the aerodynamic theory of wing sections it is possible to define the incidence angle, α_i, the angle between the principal axis z' and the direction of motion, represented as the particle slip velocity, ($\mathbf{u}$-$\mathbf{v}$), see Fig. 1 (right). At every time step (or iteration), a new α_i is based on the instantaneous particle orientation. Mathematically, the new α_i is obtained from the transformation of ($\mathbf{u}$-$\mathbf{v}$) with the third row of the elements of the orientational matrix $\mathbf{A}$ of Eq. 3. The projected area may be several orders of magnitude different from one orientation to another. The drag coefficient also varies significantly depending on the orientation. In C_D, Eq. (11), the dynamic equal-projected area circle diameter, d_n (Eq. (12)) is a function of A_D and has to be updated for every incidence angle, α_i. The lift coefficient C_L in Eq. (8) is determined such that the ratio of lift to drag forces satisfies the relationship [2]:

$$\frac{|C_L|}{|C_D|} = |\sin^2 \alpha_i \cos^2 \alpha_i| \quad (13)$$

Hence, a common approach used in the literature is to assume that the profile lift is proportional to the drag, and that the dependence with the orientation is given by the so-called 'cross-flow principle' [4, 15]. Based on this, the approach of Yin et al. [2] has been adopted, with the limitations of this approach discussed in detail elsewhere [4]. Essentially, however, the approach is valid for Reynolds numbers up to 10^3, although due to the scarcity of data at high Reynolds numbers, it is assumed that the cross-flow principle is valid for all Reynolds numbers. Rosendahl [16] reported that the validity of this principle held for different super-elliptic particles up to a Reynolds number of 1500. Mando and Rosendahl [4] also carried out sensitivity analyses on the lift/drag coefficient ratio at different Reynolds numbers with data from Rosendahl [16] and Hölzer and Sommerfeld [17] for a spheroid with relatively low aspect ratio, observing that the cross-flow principle provided a reasonable fit to data at Reynolds numbers in the Newton law

regime, with the maximum lift/drag ratio diminishing as the Reynolds number decreased. Based on this, the approach described is adopted, in which the validity is reported for Reynolds number up to 1500.

The rate of change with time of the principal components of the angular velocity $\boldsymbol{\omega} = (\omega_{x'}, \omega_{y'}, \omega_{z'})$ is given by the Euler equation as:

$$I_a \frac{d\omega_a}{dt} = T_a + (I_b - I_c)\omega_b\omega_c \tag{14}$$

where $(a,b,c) = (x',y',z')$, (y',z',x') and (z',x',y') are the principal components of the torque, T_a, the moment of inertia, I_a, and the angular velocity, ω_a. The net torque acting on the particle is caused by the non-coincident centres of mass and of pressure, $\mathbf{T}_1$, and the torque due to the resistance on a relatively rotating body, $\mathbf{T}_2$, which always act to attenuate the relative rotation. $\mathbf{T}_1$ is given in the particle frame of reference as [2]:

$$\mathbf{T}_1 = \mathbf{A}[(x_{cp}\mathbf{z}') \times (\mathbf{F}_D + \mathbf{F}_L)] \tag{15}$$

The components of torque $\mathbf{T}_2$ in a non-uniform flow field were derived by Yin et al. [2], and it is given in the absence of fluid rotation with respect to the x-axis in the particle frame of reference as:

$$\mathbf{T}_{2,x'} = \tfrac{1}{64} C_D \rho_f \times 2a \times \omega_{x'}^2 \times (2c)^4 \tag{16}$$

The components of $\mathbf{T}_2$ in the other two axial directions are obtained similarly to Eq. (16). Note that when $\cos\alpha_i > 0$, $\mathbf{T}_1$ will change its sign, such that $\mathbf{T}_1 = -\mathbf{T}_1''$, while the resultant sign in Eq. (16) takes the same sign as that of $(\mathbf{A}\boldsymbol{\omega}_f - \boldsymbol{\omega}_p)$.

The distance between the particle centres of mass and pressure, x_{cp}, was derived from airfoil theory in which the centre of pressure is approximately located a distance of one quarter of the chord length behind the leading edge for a multitude of profiles, and is valid for inclination angles in the range 0-15°. Yin et al. [2] suggested a modification of the expression for shapes with smaller aspect ratios relative to airfoils, and for inclination angles larger than 15°, and hence defined x_{cp} as a function of the aspect ratio and incidence angle as:

$$x_{cp} = 0.25c(1 - e^{3(1-\lambda)}) \, |\cos^3\alpha_i| \tag{17}$$

Lastly, the time derivative of the quaternions may be expressed as a function of the particle angular velocity, $\boldsymbol{\omega} = (\omega_{x'}, \omega_{y'}, \omega_{z'})$, in the particle reference frame as:

$$\dot{\mathbf{q}} = \begin{pmatrix} \dot{q}_1 \\ \dot{q}_2 \\ \dot{q}_3 \\ \dot{q}_0 \end{pmatrix} = \frac{1}{2} \begin{pmatrix} q_o\omega_{x'} - q_3\omega_{y'} + q_2\omega_{z'} \\ q_3\omega_{x'} + q_0\omega_{y'} - q_1\omega_{z'} \\ -q_2\omega_{x'} + q_1\omega_{y'} + q_0\omega_{z'} \\ -q_1\omega_{x'} - q_2\omega_{y'} - q_3\omega_{z'} \end{pmatrix} \tag{18}$$

8

Lastly, it should be noted that there is coupling between the translational and rotational motion. In Eq. (15), the torque due to the non-coincident centres of mass and of pressure, $\mathbf{T}_1$, is a function of the hydrodynamic force in the inertial frame which is transformed to the particle frame by the transformation matrix $\mathbf{A}$. For each time or integration step, the transformation matrix is obtained from the new quanternions, and these quaternions are subsequently used to obtain new values of α_i, A_D, d_n, C_D, F_D and $\mathbf{T}_1$. This is also the case for the torque due to the resistance on a relatively rotating body, $\mathbf{T}_2$.

3 Numerical Solution

The channel flow shown in Fig. 2 has the configuration: inertial co-ordinates ($x \times y \times z$), computational domain size ($2h \times 2h\pi \times 4h\pi$) and grid nodes ($81 \times 80 \times 80$) in the wall normal, spanwise and streamwise directions, respectively. The Reynolds numbers $Re_\tau(=hu_\tau/v)$ and $Re_b(=hu_b/v)$ were 300 and 4910 based on the shear velocity, u_τ=0.235 ms^{-1}, and the bulk velocity, $u_b \cong 3.855$ ms^{-1}, with the channel half width h=0.02 m, kinematic viscosity v=1.57×10^{-5} m^{2}s^{-1} and density ρ_f=1.3 kgm^{-3}. The mesh spacing was uniform in the y and z directions, but stretched in the x direction by a hyperbolic stretching function. Non-dimensional values of parameters associated with length, velocity and time are presented in wall units ($^+$) following normalisation with u_τ and v. Periodic boundary conditions were used in the streamwise and spanwise directions. In the streamwise direction, a mean pressure gradient was imposed as a source term to drive the flow in order to maintain a constant mass flow rate. To avoid laminarisation of the flow, an initial simulation at high Reynolds number was carried out and the resulting solution used to initialise flow at Re_τ=300. The computed mean wall shear stress was monitored and flow statistics were sampled once the shear stress became statistically steady. The computational domain, fluid and particle properties were chosen to be in line with the direct numerical simulations, and Lagrangian particle tracking of spherical particles, in a channel flow performed by Marchioli et al. [18], used for validation purposes below.
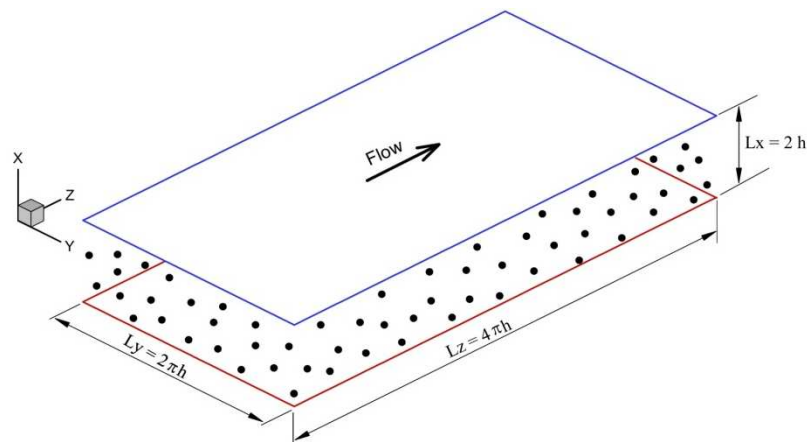

Figure 2: Computational domain

The computations were carried out with the BOFFIN large eddy simulation (LES) code [19]. The code implements an implicit finite-volume incompressible flow

solver using Cartesian co-ordinates and a co-located variable storage arrangement. Time advancement is performed using an implicit Gear method for all transport terms with variable time step, and the overall procedure is second-order accurate in space and time. For the convection terms an energy conserving discretization scheme is used and matrix pre-conditioned conjugate gradient methods are employed to solve the equations for pressure and velocity. The code has been applied extensively in the LES of reacting and non-reacting turbulent flows, e.g. [20, 21], and further details of the computational algorithms can be found in [19].

The particle equations of linear and angular momentum were both integrated using a fourth-order Runge-Kutta scheme, with the particle integration time for translation and rotation equal to 10^{-1} and 10^{-3} times the LES time step, respectively. The particles were initially randomly distributed over the computational domain, while their initial orientation was fixed as $\theta_0 = 60^{\circ}$ and $\phi_0 = \psi_0 = 0$. During each time step, the fluid flow field was first updated and then interpolated to the particle position using a trilinear interpolation scheme, with the velocity at the particle position then passed to the Lagrangian particle tracker. The initial linear velocity vector of the particles was set equal to the fluid velocity vector at the particles' position, while the angular velocity was set to zero. Similar to the fluid flow, periodic boundary conditions were imposed in the streamwise and spanwise directions to reintroduce particles exiting these boundaries back into the computational domain. The channel walls were assumed to be smooth, and perfect elastic collisions at the wall were applied. Not many realistic particle-wall interaction models for ellipsoidal particles are available in the literature. In the absence of such models, the well-known interaction model for spherical particles was assumed. When a particle wall-normal distance was less than or equal to half the particle equivalent volume diameter, the particle collision condition was assumed to be met. The sign of the particle velocity component in the wall normal direction is changed following collision, while other velocity components remain unchanged; the angular momenta remained unchanged as well. This method oversimplifies the physics of particle-wall interaction for an ellipsoidal particle, however, it is has been adopted elsewhere in the literature, e.g. [22], and provides a reasonable approach in the absence of more realistic alternatives.

Three types of particle shape representing a disk, a sphere and a needle-like particle were considered, with all the particles having an equivalent volume diameter to a sphere with a Stokes number $St = \tau_{\text{p,eq}}^{+} = 125$. Table 2 gives the values of all the particle shape and size parameters used in the simulations. The particle principal axis is taken as the z-direction with its aspect ratio as c. The size of the particles in each direction is given by $d_{\text{Veq}} = 2a(E)^{1/3}$, with $b=a$ and $c=aE$. Only the particle simulation parameters given in Table 2 were used in deriving the results presented below. Also, only the filtered velocity field was employed in calculating the particle acceleration, thus neglecting the effect of the sub-grid scale velocity fluctuations on that acceleration. At a low Reynolds number, however, Armenio et al. [23] reported that the unresolved velocity field was found to have a limited effect on the statistics of inertial particles. Therefore, the neglect of sub-grid scale velocities, in the near-wall region in particular, can be expected to have a limited influence on the results for the case of a low $Re_{\tau} = 300$ flow with high inertia $St = 125$ particles.

The different shaped particles were injected into the flow at low particle volume fraction, i.e. α_p=6.3×10⁻⁵, hence particle-particle interaction effects were neglected given that α_p=<10⁻³.

Table 2: Characteristics of the particles used in the simulations.

Case	Shape	$\tau_{\mathrm{p},eq}^{+}$	d_{Veq} / μm	S	E
1	Disk	125	114	0.418	10^{-1}
2	Sphere	125	114	1.000	10^{0}
3	Needle	125	114	0.588	10^{1}

4 Results and Discussion

Sensitivity studies were performed varying the number and distribution of computational nodes, and the time steps, used in the computations, and these studies demonstrated that the discretisations employed in deriving the results presented below resulted in turbulence and particle statistics, in those regions of the channel of interest, that were independent of the resolutions used. It should also be noted that a greater number of nodes was used in the LES of the channel flow than in comparable studies [24, 25], with close to DNS [18] resolution in the near-wall regions.

LES results are first compared with DNS predictions [18] for the single-phase flow in Fig. 3(a) for the streamwise mean velocity, including established theoretical law of the wall profiles. Figure 3(b) contains a similar comparison for the root mean square (rms) of the velocity fluctuations in all three co-ordinate directions, with Fig. 3(c) giving results for the shear stress. There is good agreement between the LES and DNS results which gives confidence in the present computations of turbulent channel flow at moderate Reynolds number. However, the overall LES approach used tends to over-predict the DNS mean velocity profile near the log-law inner-layer region, as shown in Fig. 3(a). There is also a slight disparity between the LES and DNS results for the rms of the velocity fluctuations in the three co-ordinate directions, in Fig. 3(b), but only a minor under-prediction of the shear stress peak magnitude within the buffer layer, as shown in Fig. 3(c). The rms and shear stress results given in Figs. 3(b) and 3(c) are resolved values which were computed directly from the predicted instantaneous velocities. Consideration of the contribution of sub-grid scale fluctuations may improve these comparisons, as would increases in the grid resolution used in the computations. Nevertheless, the results shown are sufficiently accurate to warrant their use in the studies of particle transport in this flow reported below.

Particles with the three aspect ratios given in Tables 1 and 2, considered to represent a disk (E=0.1), and spherical (E=1) and needle-like (E=10) particles following the Loth [11] classification, were next introduced into the flow. In order to monitor the effect of shape on particle behaviour, two groups of simulations were carried out. The first group involved the dynamics of single particles, with the three spheroids initially released from the channel inlet plane at two different

wall-normal positions (x^+=0.96 and 300) and at a fixed spanwise location (y^+=930). The three particles had the same relaxation time, $\tau_{eq}^+ = 125$, on the basis of equal equivalent volume diameter and equal mass. The starting positions chosen along the wall-normal direction are significant in wall-bounded turbulent flows as they respectively represent locations near-wall and at the centre of the channel.
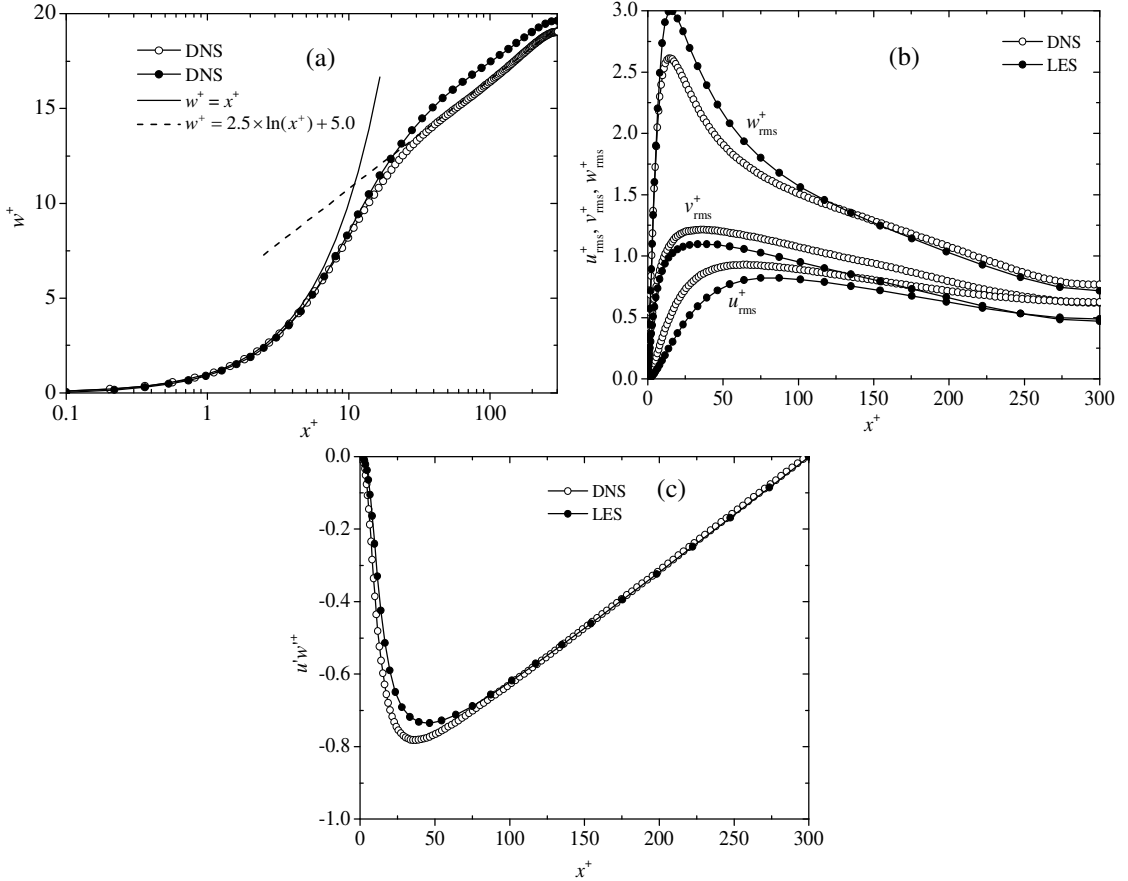

Figure 3: Validation of LES of channel flow at Re_τ=300 against DNS: (a) streamwise mean velocity with established theoretical law of the wall profiles (solid lines), (b) rms of velocity fluctuations and (c) shear stress.

Sample trajectories of the three spheroids are presented in Fig. 4, with the time history of the particle centroid position along the wall-normal and spanwise directions given for particles injected at the two locations noted above. Results in this, and subsequent figures, are given up to values of t^+=700, although it should be noted that continuing the simulations for longer times did not affect the conclusions reached below. The results of Fig. 4 provide a means of determining the deviation of non-spherical particle behaviour from that of spherical particles in a channel flow. Broadly speaking, the sphere, disk and needle-like particles all have similar paths at the beginning of the simulation, but separate from one another with time. Interestingly, the trajectories of the disk and needle-like particles are characterized by a high dispersion when compared to that of the sphere.

The differences in dispersion between the spherical and non-spherical particles are large in the wall-normal and spanwise directions close to the wall. Even after t^+=700, the spherical particle has only moved an average distance Δx^+ (Fig. 4 top

12

left) and Δy^+ (Fig. 4 top right) of less than 10, while the non-spherical particles have covered average distances of Δx^+ and Δy^+ greater than 100. This is even the case in the homogeneous spanwise direction (Fig. 4 top right) where notable differences in particle behaviour occur for the three shapes. Close to the centre of the channel (Fig. 4 bottom) these differences between the spherical and non-spherical particles are less evident, although significant variation still exists between the trajectories of the three spheroids. These results demonstrate that accounting for particle shape and orientation significantly influences the way particles translate under the influence of external forces in a channel flow.
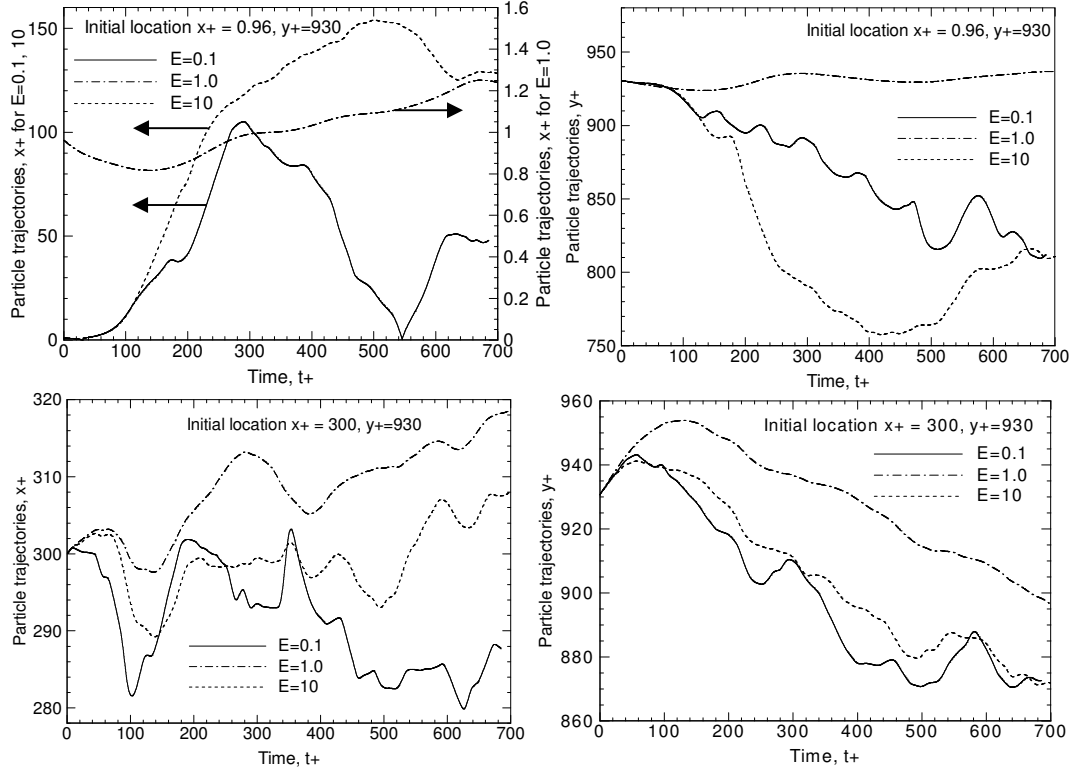

Figure 4: Time history of particle trajectories in the wall-normal (left) and spanwise (right) directions, all monitored from initial positions x^+=0.96 (top) and x^+=300 (bottom).
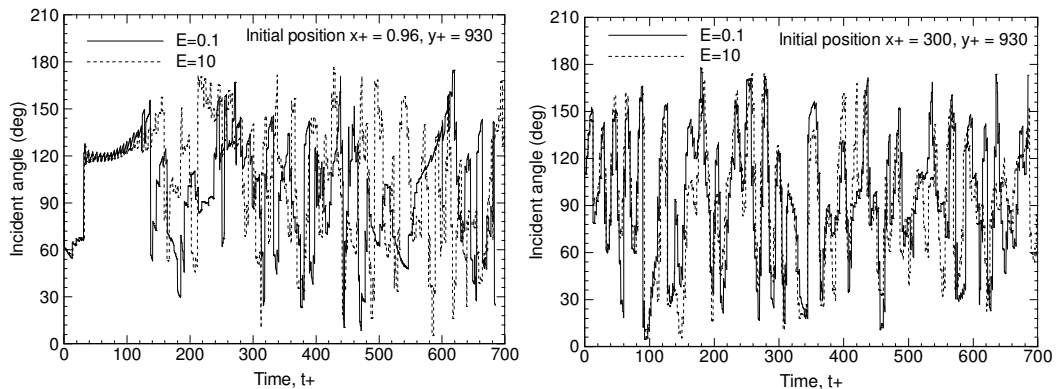

Figure 5: Time history of incidence angle between particle relative velocity and particle major axis z' monitored from initial positions x^+=0.96 (left) and x^+=300 (right).

Figure 5 shows the incidence angle, an indication of the orientation history of the non-spherical particles, monitored from initial positions of x^+=0.96 (left) and 300 (right), giving samples of non-spherical particle behaviour under the action of

13

aerodynamic forces and torques in the turbulent channel flow. The incidence angle values for the non-spherical particles are seen to oscillate around $\alpha_i = 90^o$, while that of the sphere is constant at 90° and hence not included in Fig. 5. As shown later in terms of a probability density function (PDF) plot, this dominant orientation ($\alpha_i = 90^o$) is the stable equilibrium state, as also reported in [2] for the motion of PVC particles in a non-uniform flow field. There is also similarity in the frequency and amplitude of the incidence angle monitored from both initial positions in Fig. 5, except at the beginning of the simulation (t^+<120) when the particles close to the wall are still within the viscous sub-layer (Fig. 5 left). Figure 6 shows the angular velocities with respect to the particle minor axes x' and y' for the non-spherical particles, an indication of the rotation history, again monitored from initial positions of x^+=0.96 and 300. As rotation is shape and orientation dependent, it is not considered for the spherical particle. These results demonstrate that non-spherical particles show a similar rotation history, though in opposite directions, for both particle minor axes x' and y'.
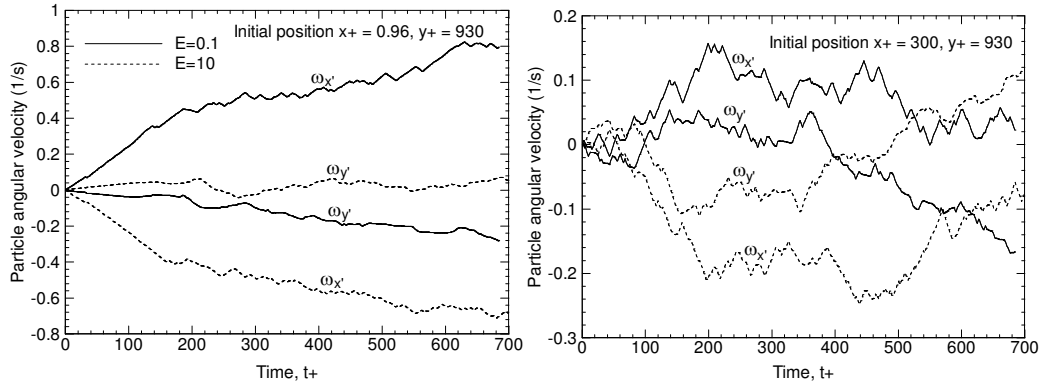

Figure 6: Time history of particle angular velocity with respect to particle minor axes x' and y' monitored from initial positions x^+=0.96 (left) and x^+=300 (right).

The second group of simulations involved monitoring 100,000 particles with initial positions randomly distributed within the channel. In these simulations, the particles were sampled in three regions: the near-wall (x^+=0.96 and 5), the buffer region (x^+=11.6 and 30) and at the channel centre ($x^+ = 300$), with the results presented in the form of probability density functions below. The simulations of the multiple particles were run for $t^+ \sim 25,400$, with statistical sampling to derive the PDFs shown carried out after $t^+ = 125$ at intervals of $t^+ = 10$, resulting in time-independent statistics. It should be noted that the sample volume used was relatively small, and hence the variation of particle parameters might also be expected to be small. However, when the influence of particle rotation is considered, a significant level of variation in the PDFs of those variables monitored is anticipated.
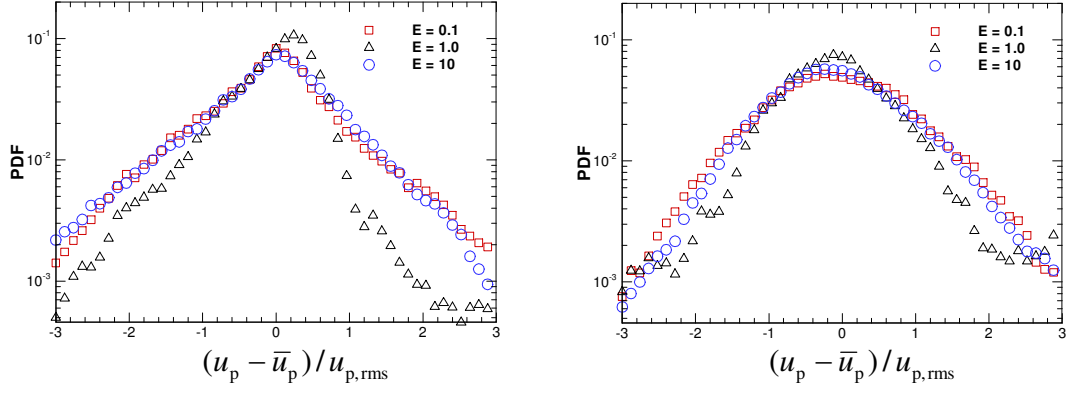
Figure 7: PDF of normalised wall-normal particle velocity, sampled at x^+=11.6 (left) and x^+=300 (right).
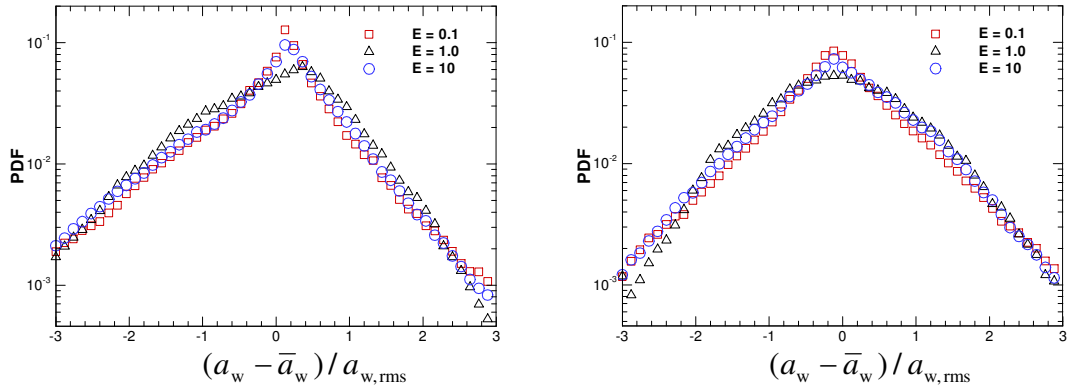

Figure 1: PDF of normalised wall-normal component of particle acceleration, sampled at x^+=11.6 (left) and x^+=300 (right).

PDFs of the normalised wall-normal particle velocity, $(u_p - \bar{u}_p)/u_{p,rms}$, are shown in **Error! Reference source not found.**, with results for the normalised wall-normal component of the particle acceleration, $(a_w - \bar{a}_w)/a_{w,rms}$, shown in

Figure 1, both sampled at locations of x^+= 11.6 and 300. A semi-logarithmic scale is used for the PDFs to emphasise the shape of the tails. It is seen that the PDF of the particle wall-normal velocity in the buffer region is less symmetric with respect to 0 than the PDF of the particles at the channel centre**Error! Reference source not found.**. Also, although there is some similarity between the frequency of the particle velocity for the two non-spherical particles, differences are apparent between these particles and their spherical counterparts. These differences are seen at both sample locations, although they are less significant at the channel centre. The peak in the PDF of the normalised wall-normal velocity is also clearly higher for the spherical particles at both locations, implying an increased probability of finding spherical particles with a zero wall-normal velocity. These results imply that it is likely, with further simulation time, that particle preferential concentration at the walls of the channel will vary depending on the particular particle shape, although further work is required to quantify such effects. For the normalised wall-normal acceleration results of Fig. 8, differences between the different particle types are less apparent than for the wall-normal particle velocity. The tail of the PDFs is therefore similar for all the particles, although differences do occur between the various shapes, especially at the peak values where $(a_w - \bar{a}_w)/a_{w,rms} = 0$.
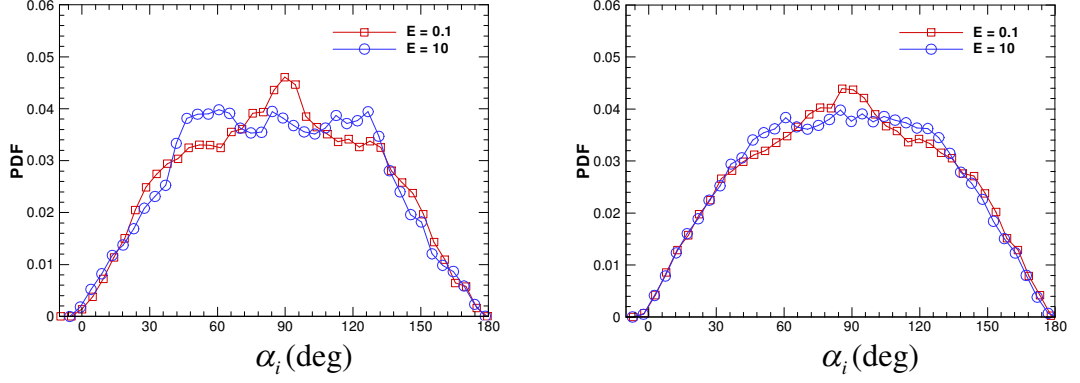
15

Figure 9: PDF of particle incidence angle, α_i, for the disk and needle-like particles, sampled at $x^+=11.6$ (left) and $x^+=300$ (right).

PDFs of the particle incidence angle α_i for particles with $E=0.1$ and $E=10$, again sampled in the buffer region and at the channel centre, are shown in **Error! Reference source not found.**. The incidence angle is a measure of the particle orientation that is included in the drag and lift force calculations. Both plots are symmetrical with respect to $\alpha_i = 90^{\circ}$. The results demonstrate that the non-spherical particles assume orientations with incidence angles ranging from 0° to 180°, although $\alpha_i = 90^{\circ}$ is the most probable for situations where the fluid rotation is neglected, as previously observed in the results of **Error! Reference source not found.** and in [2] for settling cylindrical particles in a non-uniform flow.
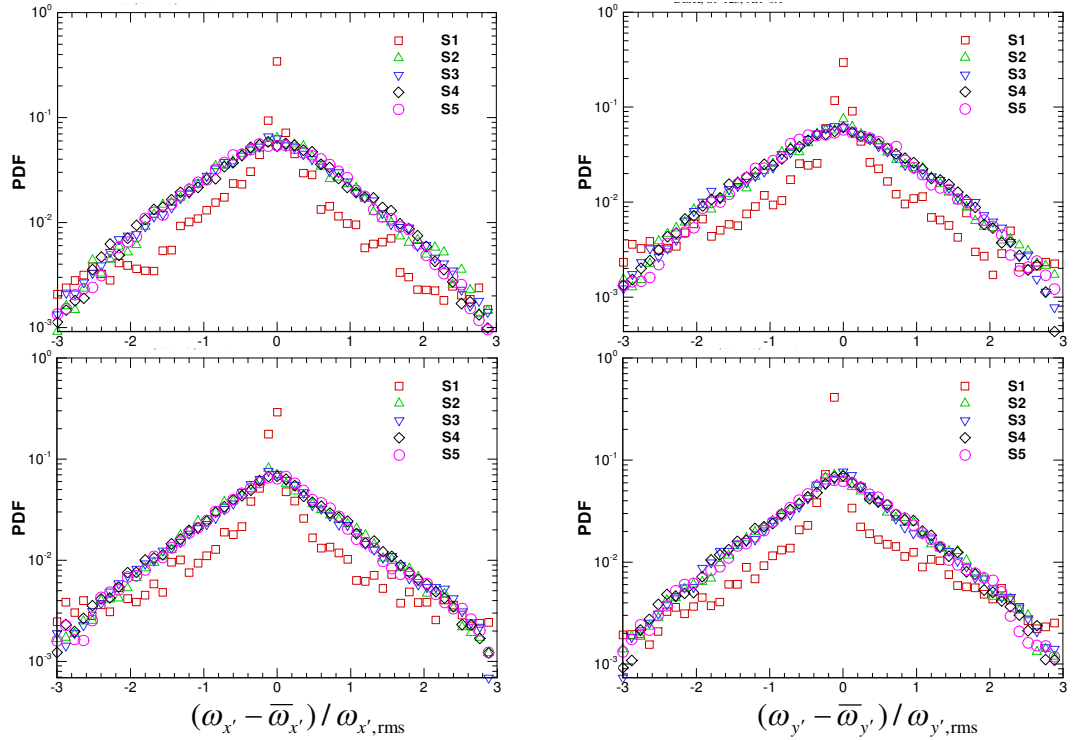

Figure 2: PDF of normalised particle angular velocity with respect to the minor axes x', $(\omega_{x'} - \overline{\omega}_{x'})/\omega_{x',\mathrm{rms}}$ (left), and y', $(\omega_{y'} - \overline{\omega}_{y'})/\omega_{y',\mathrm{rms}}$ (right), for disk (top) and needle-like (bottom) particles. Series (S1, S2, S3, S4, S5) = sample location ($x^+ = 0.96, 5, 11.6, 30, 300$).

16

Normalised particle angular velocity probability density functions at five wall-normal locations ($x^+ = 0.96, 5, 11.6, 30, 300$) are shown in

Figure 2 with respect to the particle minor axes x' and y', and for disk and needle-like particles. The plots show, for both particle shapes, that the angular velocity takes on a distinct shape with respect to the boundary layer region. In all the plots, therefore, the angular velocity components with respect to both particle minor axes show the largest peak values at the mean of the distribution for sample locations closest to the wall. In the buffer region, at $x^+=11.6$ and 30, the PDFs show similar, although lower, peaks, as well as similar distribution tails in both the x' and y' directions, for both particle shapes. Towards the centre of the channel, where the particles experience less shear from the fluid flow, the PDF of the angular velocity shows a symmetric profile. As the non-spherical particle size was characterised by the volume equivalent diameter, d_{Veq}, the particles have equal volume, density, mass and Stokes number. This is likely the reason for the small differences observed between particle types, with in some cases no difference at all in the particle properties being apparent. In addition, the non-inclusion of fluid rotation in computing the particle torque due to resistance may have led to similar particle rotational distributions in the buffer region and at the turbulent core, with the differences at the near-wall due to particle collisions with the solid surface.
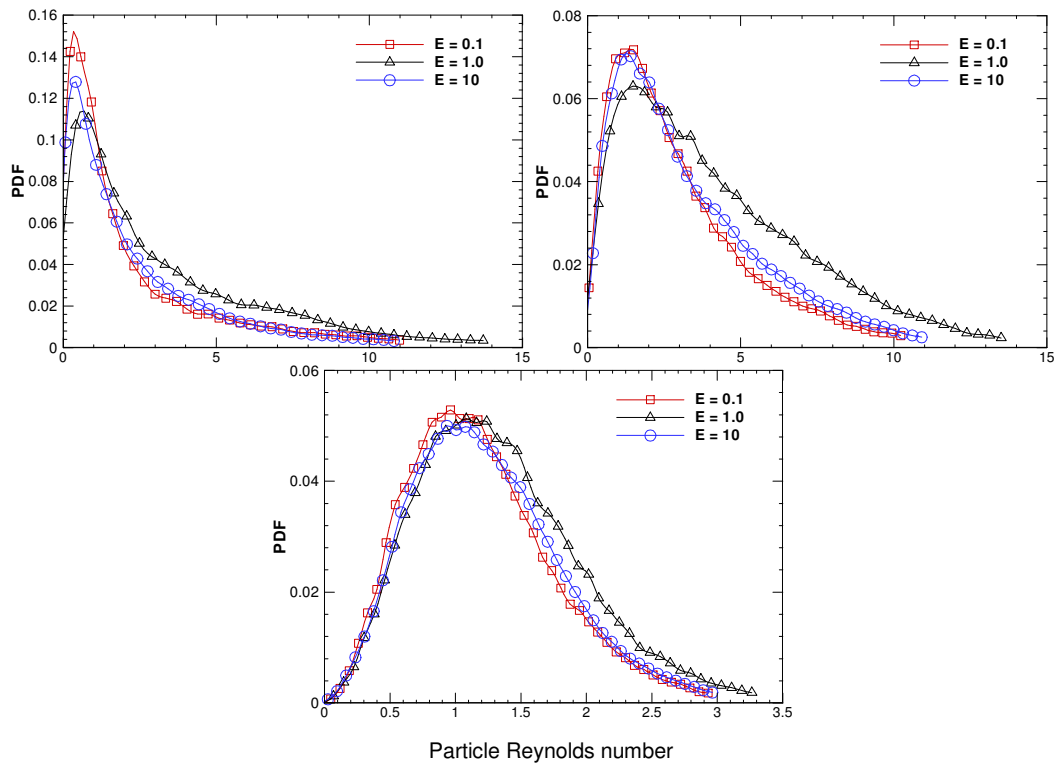

Figure 3: PDF of particle Reynolds number, Re_p, sampled at $x^+ = 5$ (upper left), 11.6 (upper right) and 300 (bottom).

Particle Reynolds number probability density functions sampled at three wall-normal locations are shown in

Figure 3 for the three shapes of particle. Small differences are observed at the channel centre, with the dissimilarity in the values of the Reynolds number increasing towards the channel wall, with the non-spherical particles showing significant differences from the spherical particles at $x^+ = 11.6$, and with the disk-like particles clearly showing the largest values at the location closest to the wall.

17

The Reynolds number is also higher for all particles in the buffer region where the relative velocity between the particles and the fluid is greater than at the channel centre where the slip velocity tends to zero.
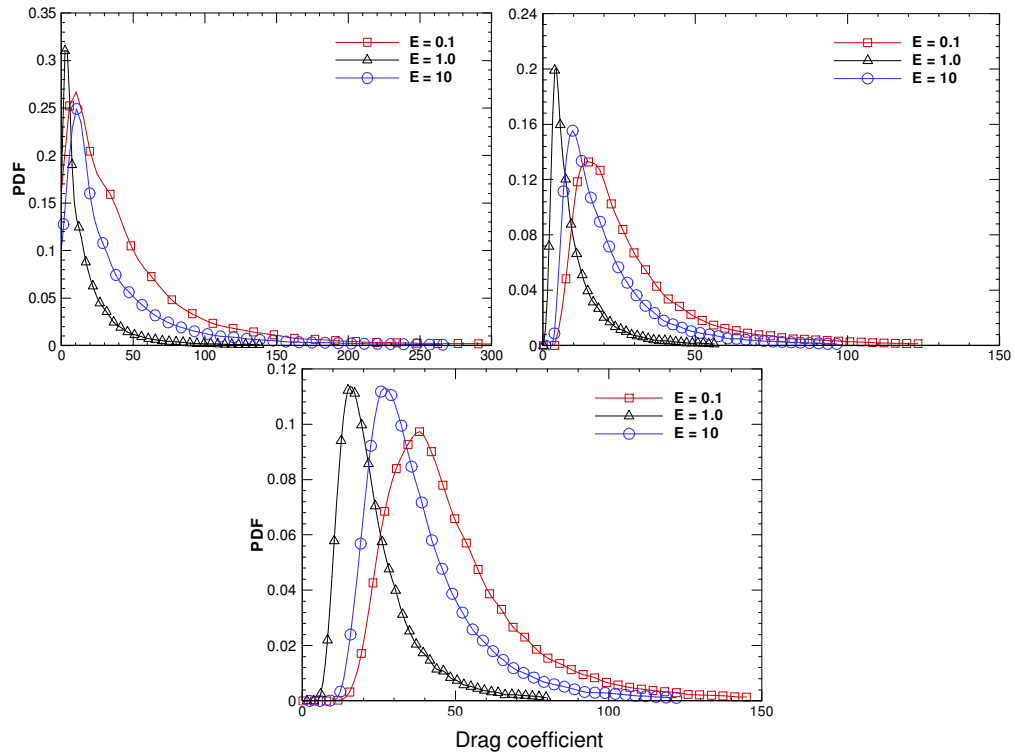

Figure 12: PDF of particle drag coefficient, C_D, sampled at $x^+ = 5$ (upper left), 11.6 (upper right) and 300 (bottom).

Lastly, **Error! Reference source not found.** shows the associated drag coefficient PDF, again sampled at three wall-normal locations. Particles with the same volume equivalent diameter at similar wall-normal locations necessarily have similar Reynolds numbers but different drag coefficients, with their shape and orientation contributing factors to this difference. The needle-like particles are seen from these results to have increased drag compared to the equivalent spherical particles, while the disk-like particles have in turn an increased drag relative to both other particle types. In addition, it can be seen that the difference in the value of the drag coefficients increases greatly with increasing particle Reynolds number. This implies that the drag coefficient is more influenced by particle shape and orientation at high Reynolds numbers, i.e. the largest differences occur at the channel centre. Also, as the particles have the same volume, and exhibit similar value of Re_p (Fig. 11) but differences in the drag coefficient (Fig. 12), it is clear that it is differences in particle rotation, due to shape, that cause the increase in drag coefficient as well as its variation.

5 Conclusions

Large eddy simulation and a Lagrangian particle tracking scheme have been used to study the influence of shape, and by extension orientation, on particle behaviour in a turbulent channel flow. The LES, with a dynamic sub-grid scale

18

model, has been shown to produce results for a low Reynolds number flow that are in acceptable agreement with a DNS of the same channel flow. Resolved velocities were subsequently used to study the behaviour of particles of differing shape, assuming one-way coupling between the fluid and the particles, with both translational and rotational motions of the particles considered by solving Newton's and Euler's equations of motion using a fourth-order Runge-Kutta scheme.

Overall, the simulations have demonstrated that the shape of a particle has an influence on its dynamics within the turbulent channel flow considered, and that particle shape should be taken into account when designing and optimising industrial systems where non-spherical particles are prevalent. The inclusion of particle shape and orientation in the formulation of the Lagrangian particle tracking approach has therefore shown, both in terms of the behaviour of single and multiple particles, that the dynamics of non-spherical particles differ from the corresponding behaviour of spherical particles with the same equivalent volume diameter and the same mass. For the wide range of applications where differing particle sizes and morphologies are of importance, and for the nuclear reactor applications of specific interest in the work described, models that account for particle shape and orientation are clearly necessary if reliable predictions of particle dispersion, deposition and re-suspension from solid surfaces are to be made. The present results also call into question the use of a spherical particle assumption in modelling such particle-laden flows since particle rotation and orientation causes variation in the drag coefficient.

As previously noted, for low Reynolds number flows it has been found that the unresolved velocity field has only a limited effect on the statistics of inertial particles [23], and hence these effects can be justifiably excluded for the case of the low Re_τ=300 flow and high inertia particles considered. However, for particles with lower Stokes numbers, which will not filter out a large spectrum of turbulent structures, it may be anticipated that sub-grid scale fluid velocities will have a more significant impact on particle translation and rotation. Future efforts will therefore consider the impact of sub-grid scale velocities on the behaviour of all the particle shapes considered over a range of Stokes numbers, as well as the influence of two-way coupling between the fluid and the particles.

Acknowledgements

References

[1] C. Yin, L. Rosendahl, S. K. Kær, T. J. Condra, Use of numerical modeling in design for co-firing biomass in wall-fired burners, Chem. Eng. Sci., 59 (2004) 3281-3292.

[2] C. Yin, L. Rosendahl, S. Knudsen Kær, H. Sørensen, Modelling the motion of cylindrical particles in a nonuniform flow, Chem. Eng. Sci., 58 (2003) 3489-3498.

[3] G.H. Ganser, A rational approach to drag prediction of spherical and nonspherical particles, Powder Technol., 77 (1993) 143-152.

[4] M. Mandø, L. Rosendahl, On the motion of non-spherical particles at high Reynolds number, Powder Technol., 202 (2010) 1-13.

[5] M. Zastawny, G. Mallouppas, F. Zhao, B. van Wachem, Derivation of drag and lift force and torque coefficients for non-spherical particles in flows, Int. J. Multiphase Flow, 39 (2012) 227-239.

[6] C. Marchioli, M. Fantoni, A. Soldati, Orientation, distribution, and deposition of elongated, inertial fibers in turbulent channel flow, Phys. Fluids, 22 (2010) 033301-033314.

[7] L. Tian, G. Ahmadi, Z. Wang, P.K. Hopke, Transport and deposition of ellipsoidal fibers in low Reynolds number flows, J. Aerosol Sci, 45 (2012) 1-18.

[8] H. Zhang, G. Ahmadi, F.-G. Fan, J.B. McLaughlin, Ellipsoidal particles transport and deposition in turbulent channel flows, Int. J. Multiphase Flow, 27 (2001) 971-1009.

[9] R. Hazelton, Characteristics of Fuel Crud and its Impact on Storage, Handling, and Shipment of Spent Fuel, in, 1987.

[10] J.E. Hilton, P.W. Cleary, The influence of particle shape on flow modes in pneumatic conveying, Chem. Eng. Sci., 66 (2011) 231-240.

[11] E. Loth, Drag of non-spherical solid particles of regular and irregular shape, Powder Technol., 182 (2008) 342-353.

[12] U. Piomelli, J. Liu, Large-eddy simulation of rotating channel flows using a localized dynamic model, Phys. Fluids, 7 (1995) 839-848.

[13] H. Goldstein, Classical Mechanics, 2nd ed., Addison-Wesley, Reading, MA, 1980.

[14] R.P. Chhabra, L. Agarwal, N.K. Sinha, Drag on non-spherical particles: an evaluation of available methods, Powder Technol., 101 (1999) 288-295.

[15] S.F. Hoerner, H.V. Borst, Fluid dynamic lift: practical information on aerodynamic drag and hydrodynamic resistance, Brick Town, New Jersey, 1975.

[16] L. Rosendahl, Extending the modelling framework for gas-particle systems: Applications of multiparameter shape descriptions to non-conventional solid fuels in reacting and non-reacting environments. PhD Thesis, Aalborg University, Denmark, 1998.

[17] A. Hölzer, M. Sommerfeld, Lattice Boltzmann simulations to determine drag, lift and torque acting on non-spherical particles, Comput. Fluids, 38 (2009), 572-589.

[18] C. Marchioli, A. Soldati, Reynolds number scaling of particle preferential concentration in turbulent channel flow, in: J.M.L.M. Palma, A. Silva Lopes (Eds.) 11th EUROMECH European Turbulence Conference, Springer Proceedings in Physics 117, Springer, Heidelberg, Porto, Portugal, 2007, pp. 298-300.

[19] W.P. Jones, F. di Mare, A.J. Marquis, LES-BOFFIN: Users guide, technical memorandum, in, Mechanical Engineering Dep't, Imperial College of Science, Technology and Medicine, London, UK, 2002.

[20] M. Bini, W.P. Jones, Large-eddy simulation of particle-laden turbulent flows, J. Fluid Mech., 614 (2008) 207-252.

[21] D.O. Njobuenwu, M. Fairweather, Large eddy simulation of particle-laden flow in a duct with a 90° bend, J. Phys: Conf. Ser., 318 (2011) 042058.

[22] P.H. Mortensen, H.I. Andersson, J.J.J. Gillissen, B.J. Boersma. Dynamics of prolate ellipsoidal particles in a turbulent channel flow. Phys. Fluids, 20 (2008) 093302.

[23] V. Armenio, U. Piomelli, V. Fiorotto, Effect of the subgrid scales on particle motion, Phys. Fluids, 11 (1999) 3030-3042.

[24] C. Marchioli, M.V. Salvetti, A. Soldati, Some issues concerning large-eddy simulation of inertial particle dispersion in turbulent bounded flows, Phys. Fluids 20 (2008) 040603.

[25] Q. Wang, K. D. Squires, Large eddy simulation of particle-laden turbulent channel flow, Phys. Fluids 8 (1996) 1207-1223.